

# Maneuver estimation from optical observations of a spiraling orbit: the case of MEV-2

**Laura Pirovano**

*Te Pūnaha Ātea - Space Institute, University of Auckland, New Zealand*

**Roberto Armellin**

*Te Pūnaha Ātea - Space Institute, University of Auckland, New Zealand*

## ABSTRACT

Building and maintaining knowledge of resident space objects involves several tasks, ranging from observations to data analysis. Once acquired, the knowledge of a space object needs to be updated following a dedicated observing schedule. Dynamics mismodelling and unknown maneuvers can however alter the accuracy of the catalog, resulting in uncorrelated observations originating from the same object. This paper presents the chain of algorithms to perform initial orbit determination, tentative data association assuming natural motion, orbit determination, and finally maneuver estimation for optical observations of MEV-2 during orbit raising. The algorithms make use of high-order methods and the maneuver is estimated through convex optimization without a-priori assumptions on the thrust arcs structure and thrust direction.

## 1. INTRODUCTION

During April 2021, the Mission Extension Vehicle-2 (MEV-2) spacecraft completed rendezvous and docking with INTELSAT 10-02 as part of a commercial life-extension mission in geostationary Earth orbit (GEO). Researchers from the Five-Eyes (FVEYs) community, within the Phantom Echoes-2 (PE2) experiment, conducted a series of observation campaigns to study the low-thrust (LT) orbit raise of MEV-2 from geostationary transfer orbit (GTO) to GEO and the behaviors of the two satellites to improve allied capabilities for the protection of spacecraft in GEO. Te Pūnaha Ātea - Space Institute (TPA-SI) aided in the data processing part of the experiment by performing initial orbit determination (IOD), data association, orbit determination (OD) and maneuver estimation for observations collected by Defence Technology Agency (DTA). This paper will show the algorithm chain which brought to the estimation of the time-profile of the LT orbit raise maneuver performed by MEV-2 starting from a series of optical observations. Section 2 gives the mathematical details our current capabilities in terms of IOD, data association, OD and maneuver estimation algorithms, which constitute the core of our catalog build-up and maintenance capability. Section 3 shows the intermediate outputs and final time-profile and Probability Density Function (PDF) reconstruction for the estimated maneuvers. Conclusions and future work are included in Section 4.

## 2. MATHEMATICAL BACKGROUND

This section presents the mathematical grounds developed to obtain an orbit starting from a series of optical observations. It is to be noted that Differential Algebra (DA)<sup>1</sup> is used to implement high-order methods throughout the section. Section 2.1 introduces two IOD methods, the Admissible States Region (ASR) [8] and the Orbit Set (OS) [9], which estimate an analytical uncertainty region given an optical observation, from here on called *track*. The former is used when tracks are very-short arcs (VSAs), while the latter allows for the definition of a state guess for longer tracks. Section 2.2 then introduces a data association process called range intersection [8, 10], which is enabled by the high-order definition of the uncertainty. The method establishes whether two tracks can be linked to the same Resident Space Object (RSO) assuming natural motion. This is performed to understand whether non-associated VSAs, known as Uncorrelated Tracks (UCTs), can be linked to newly acquired tracks. If successful, a tentative OD can be performed

---

<sup>1</sup><https://github.com/dacelib/dace>

to find the orbit which fits in the two IODs, otherwise the new track is placed in the UCTs pool, if it is a VSA. Section 2.3 describes the Differential Algebra Least Squares (DALs) [4], a high-order Least Square (LS) solver which performs OD either refining an IOD when the track is not a VSA, or confirming association following a successful range intersection. The DALs outputs a state and a covariance. Lastly, Section 2.4 explains the convex-optimization based maneuver estimator, which takes as input the outputs of two ODs and tries to recover association assuming a maneuver has happened, once correlation under natural motion assumption is discarded with the range intersection. If successful, a maneuver profile is estimated, otherwise non-correlation is concluded and the two ODs belong to two different satellites. The relation between algorithms is shown in Fig. 1.

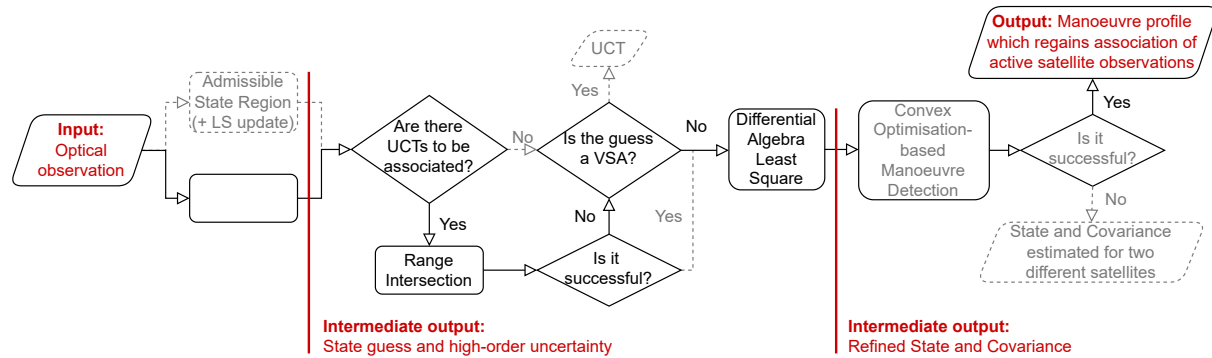


Fig. 1: Flowchart of the algorithms chain which brings from an optical observation to the estimation of the maneuver profile through IOD and OD. Dashed grayed paths are not considered in this paper but are included for sake of completeness.

## 2.1 Initial Orbit Determination: Admissible State Region and Orbit Set

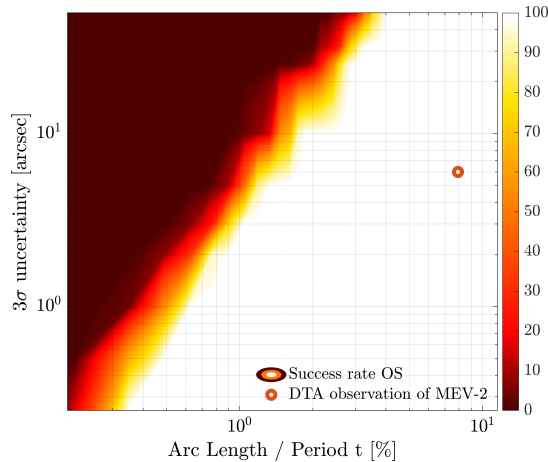


Fig. 2: Success rate of OS algorithm, modified from [9].

Depending on the length and precision of the track, different algorithms can be used to extract as much information as possible from it. Usually algorithms such as Gauss and Lambert are used to obtain an initial guess for the state. However, if a track is a VSA, too little information is available to obtain a state guess, and the Admissible Region (AR) [6] approach is the typical method used, where instead of fitting an orbit through the observations, the uncertainty is bounded with energy and orbital constraints. From these two methods, two new algorithms were created which use high-order methods to not only define the guess but also to analytically describe the uncertainty: the ASR from the AR, and the OS from literature IOD algorithms. Fig. 2 shows the success rate of the OS algorithm depending on the track length and precision. For very low success rates (dark red area), the ASR is used. As can be seen in Fig. 2, the observations of MEV-2 are long enough to obtain an OS. It was indeed a tracking effort rather than a surveillance campaign. Nevertheless, an update of the ASR algorithm is also included in the following discussion, to show how the ASR and the OS converge to the same conclusion when more information is available.

### 2.1.1 Admissible State Region

To obtain an initial guess for VSAs, the set of observations  $(t, \alpha, \delta, \sigma)_i$  for  $i \in \mathbb{N}_{[1, N]}$  - comprising time  $t$ , right ascension  $\alpha$ , declination  $\delta$  and their precision  $\sigma$  - is linearly regressed at a center point (C), where the regressed quantities and

their derivatives are saved  $(\alpha_C, \delta_C, \dot{\alpha}, \dot{\delta})$ . The two remaining degrees of freedom (DoF)  $(\rho, \dot{\rho})$  are then bounded with energy and orbital constraints. Adding on to the literature available, we used high-order techniques [8] to analytically describe the uncertainty of the AR and attributable, reaching the concept of ASR, where the 6D uncertainty is described with a list of polynomials. The gray boxes in Fig. 3 show the 2D projection of the ASR on the AR (solid gray lines) for a GEO object, with initial bounds  $20000 \text{ km} \leq a \leq 45000 \text{ km}$  and  $e \leq 0.78$ . The discretization in boxes is needed to keep an accurate analytical definition within the sub-domains, and it is automatically performed by the Automatic Domain Splitting (ADS) [11] while creating the ASR. Having a polynomial expression of the uncertainty within the domains, it is easy to estimate the bounds of the uncertainty for each domain, which is exploited for data association, as explained in Section 2.2. When more observation than just 3 (the minimum required to perform linear regression) are available, it is possible to update the ASR by calculating the minimum residual between the real observations and the expected ones, which are in polynomial form, effectively looking for the minimum of the function over each sub-domain.

Equation (1) shows the residual function, using the  $i$ -th observation over the  $j$ -th sub-domain:

$$[r_{i,j}] = \frac{1}{2} \left( \frac{\alpha_i - [\alpha_i]}{\sigma_i} \right)^2 + \left( \frac{\delta_i - [\delta_i]}{\sigma_i} \right)^2 \Big|_j \quad (1)$$

where  $[\square]$  indicates the polynomial form of the variable. Boxes with high residuals are then discarded with two filters: firstly by checking the polynomial range of the residual, which is a coarse but very fast filter, then using the Broyden-Fletcher-Goldfarb-Shanno (BFGS) algorithm from `dlib`<sup>2</sup>, more time consuming, but only applied on a small portion of remaining domains. Following this routine it is possible to prune up to 90% of the uncertainty region for tracks which fall in the red area of Fig. 2 [8]. This can be done either sequentially or with a batch LS. An example of the sequential pruning is shown with the colored boxes in Fig. 3. For MEV-2 observations, the batch approach will be shown in the result, given the large number of observations in each track.

### 2.1.2 Orbit Set

When tracks fall in the white region of Fig. 2, it is possible to obtain a candidate state guess by fitting a keplerian orbit through three observations. By picking the first, middle and last observation in a track it is possible to exploit the full length of the track to obtain a candidate solution. Each angular observation, though, has a specific precision  $\sigma$ . The OS algorithm then finds all possible orbits which geometrically fit in the three observations within the specified accuracy. Again the ADS is used to control the accuracy. Equation (2) summarizes the map, where  $j$  refers to the  $j$ -th sub-domain:

$$f_{IOD+ADS} = \bigcup_j \mathcal{T}_j : (\alpha, \delta)_j \in \mathbb{R}^6 \rightarrow (\mathbf{r}_2, \mathbf{v}_2)_j \in \mathbb{R}^6, \quad (2)$$

meaning that the couples  $(\alpha, \delta)$  at  $t_1, t_2$  and  $t_3$  serve as domain to obtain a state estimate at the central time. Just like Section 2.1.1, the output is an analytical expression for which it is easy to estimate the bounds of uncertainty. When the track falls on the boundary of feasibility of Fig. 2, the size of the projected

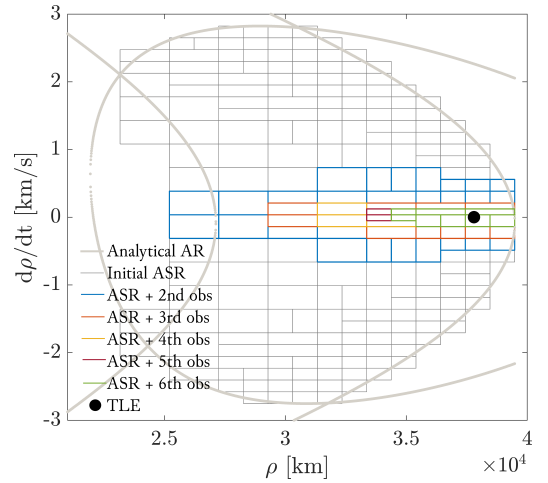


Fig. 3: Sequential update of ASR for a GEO track, modified from [8].

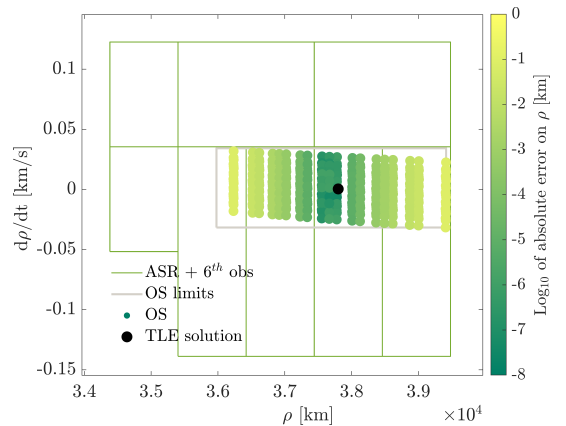


Fig. 4: OS and updated ASR from Fig. 3.

<sup>2</sup>[http://dlib.net/optimization.html#find\\_min\\_box\\_constrained](http://dlib.net/optimization.html#find_min_box_constrained)

OS tends to the size of the AR. Conversely, when more observations are available, the updated ASR tends to the size of the OS as shown in Fig. 4. In this case, only one box was enough to keep the accuracy of the polynomial expression below the 100 m threshold.

## 2.2 Data Association with natural motion assumption: Range Intersection

As can be seen in Fig. 3 and Fig. 4, for every sub-domain it is straightforward to estimate the uncertainty bounds in polar coordinates, which are plotted. By applying classical reference frame transformations, it is then possible to obtain bounds for any coordinate type, such as classical orbital elements (COE). COE are of interest thanks to their straightforward physical meaning and slow variation for small windows of time. Indeed, to compare different guesses and assess correlation, it is possible to check the 5D intersection of the slowly varying elements, under the assumption that the elements' variation within the time window considered is much smaller than the uncertainty involved. This allows for a quick correlation check, without propagation. If the intersection is the empty set, then the observations are not correlated. Otherwise, a reference orbit can be obtained within the intersection and refined through a LS.

## 2.3 Orbit Determination: Differential Algebra Least Squares

When two ASRs or OSs are correlated, or when the track is longer than a VSA - like the MEV-2 case - it is possible to refine the state guess through a LS routine which uses all observations in the track. In this work, we make use of the DALs [4], a high-order LS method which can perform OD, with the option to estimate the ballistic and solar radiation pressure (SRP) coefficients. It can handle radar and optical observations, using numerical or semi-analytical propagators. The advantage of this version with respect to literature approaches is the robustness to IOD uncertainty, and it outputs the refined state and covariance estimate.

## 2.4 Correlation Recovery with Active Satellite Assumption: Maneuver detection

If two guesses end up being uncorrelated following the range intersection method explained in Section 2.2, it means there is not a ballistic path which can connect the two states. However, the satellite may have maneuvered in the meantime, meaning an unmodeled perturbation affected the ballistic hypothesis. It is then possible to set up an optimization procedure which estimates the necessary maneuver to re-gain correlation starting from two ODs. Depending on the propulsive system and available onboard  $\Delta v$ , the problem may be feasible, meaning the two observation could be originated from the same maneuvering satellite, or infeasible, meaning the two observations are definitely not correlated. We devised a new method based on Second-Order Cone Programming (SOCP) to find the optimal maneuver profile to connect two states with uncertain bounds, their covariances, effectively solving an optimal control problem (OCP) with uncertain boundary constraints. Equation (3) summarizes the OCP with its general formulation on the left - with state  $x$ , control  $u$  and other parameters  $p$  -, and problem specific formulation on the right:

$$\min J(\delta x, u, p | x_0, x_1, t_0, t_f) \quad \min \Delta V = \int_{t_0}^{t_f} \|\mathbf{u}(\tau)\| d\tau \quad (3a)$$

$$\text{s.t. } \dot{x}(t) = f(x, \delta x, u, p, t), \quad \text{s.t. } \mathbf{a} = \mathbf{a}_{\oplus} + \mathbf{a}_{\text{drag}} + \mathbf{a}_{\odot} + \mathbf{a}_{\mathbb{C}} + \mathbf{a}_{\text{SRP}} + \mathbf{u} \quad (3b)$$

$$(x(t), u(t), t) \in \mathcal{C}(t), \quad \forall t \in \mathbb{R}_{\Delta t}$$

$$\delta x_0 \in \mathcal{X}_0, \quad \delta x_1 \in \mathcal{X}_1. \quad \frac{1}{2} \delta \mathbf{x}_j^T \Sigma_j \delta \mathbf{x}_j \leq q_{\chi^2}(\alpha, 6) = \mathcal{M} \quad j \in \mathbb{N}_{[0,1]}. \quad (3c)$$

The aim is to minimize fuel consumption (Eq. (3a)), with high-accuracy dynamics - Earth's gravity potential, drag, Sun and Moon perturbations, SRP and control - (Eq. (3b)), within the bounds set by the OD covariances in the form of the Mahalanobis distance (Eq. (3c)). It is fundamental that the natural motion of the body is accurately described, to avoid overloading the control with unmodeled known dynamics, resulting in a non-realistic  $\Delta V$  profile. In most cases the solution of such an infinite-dimensional optimization problem is neither available in closed form nor is it computationally tractable numerically (especially in real-time) [5]. Unknowable computational time and lack of assured algorithm convergence are obstacles to the reliable and rapid use of these algorithms in real applications [3]. Instead, some modification are now introduced to transform this Nonlinear Programming (NLP) problem into a SOCP

problem to exploit its feature: guaranteed convergence to a global minimum in polynomial time. A SOCP problem is in the following form:

$$\min \quad \mathbf{c}^T \mathbf{x} \quad (4a)$$

$$\text{s.t.} \quad \mathbf{A}\mathbf{x} = \mathbf{b} \quad (4b)$$

$$\|F_i \mathbf{x} + \mathbf{d}_i\| \leq \mathbf{p}_i^T \mathbf{x} + q_i, \quad i \in \mathbb{N}_{[1:L]} \quad (4c)$$

having a linear minimization function, and linear and cone constraints.

The following manipulations will bring Eq. (3) in the form of Eq. (4):

1. The problem is transformed to a finite-dimensional one by discretizing the trajectory into a finite number of nodes  $N$  and assuming that the control can only assume a fixed value between two consecutive nodes. The minimization function is thus the sum of all  $\|\Delta \mathbf{v}\|$  contributions on all nodes.
2. Typical lossless convexification procedures such as equivalent transformation and relaxation [3] are used to calculate the  $\|\Delta \mathbf{v}\|$ s as a cone constraint and hence obtain a linear minimization function.
3. At each node, variations in the accurate ballistic trajectory due to maneuvers and variation in the initial state are mapped with state transition matrices (STMs) and continuity of the trajectory is enforced:

$$\text{prop}(\mathbf{x}_i + \delta \mathbf{x}_i + \delta \mathbf{v}_i) \approx \tilde{\mathbf{x}}_{i+1} + [R_i | M_i] \begin{bmatrix} \delta \mathbf{x}_i \\ \delta \Delta \mathbf{v}_i \end{bmatrix} = \mathbf{x}_{i+1}, \quad (5)$$

where  $\tilde{\mathbf{x}}_i$  is the accurate discretized ballistic trajectory,  $i \in \mathbb{N}_{[0,N]}$  are the nodes, and  $R_i \in \mathbb{R}^{6 \times 6}$ ,  $M_i \in \mathbb{R}^{6 \times 3}$  are the STMs, which respectively map deviations in the states and velocity to the next node.

4. Continuity at the last node is enforced:  $\mathbf{x}_N = \mathbf{X}_{1,1} + \delta \mathbf{x}_1$ .
5. Lastly, the Mahalanobis distance constrain is changed. Indeed, to be able to accurately reconstruct the PDF of the maneuver,  $\delta \mathbf{x}_0$  and  $\delta \mathbf{x}_1$  cannot be optimization variables: by simply constraining the initial and final deviations to be less than a value as in Eq. (3c), the optimizer will see the deviations as “free propellant” hence taking full advantage of them, but actually creating the least probable path. Indeed, the deviations are not purely geometrical but hold a statistical meaning: the further from the mean states the final solution is, the less probable the path found is to happen. So despite Eq. (3c) being already in cone form, state variations need to be defined beforehand. The fourth-order Conjugate Unscented Transform (CUT) [2] was chosen to do so: by running the optimization  $N^2 + 2N + 1$  times, where  $N = 12$  is the dimension of the problem, it is possible to reconstruct a-posteriori the first four momenta - mean, variance, skewness and kurtosis - of the final maneuver profile distribution, thus allowing for the analysis of the effect of uncertainty in the states on the overall maneuver existence and estimation. Sigma points drawn from the initial and final covariance determine the initial and final deviations, so that Eq. (3c) is substituted by:

$$\begin{bmatrix} \delta \mathbf{x}_0 \\ \delta \mathbf{x}_1 \end{bmatrix}_c = \Delta \mathbf{X}_{CUT4,c}^{12 \times 1} \quad c \in \mathbb{N}_{[1, N^2 + 2N + 1]} \quad (6)$$

Figure 5 summarizes the procedure explained here above, where the original trajectory is modified with two example maneuvers and a variation in the initial state to match the variation in the final state. This problem can be solved by primal-dual interior-point methods. We use MOSEK through its MATLAB interface<sup>3</sup>, while DA is used to automatically compute the STMs in C++. Due to linearization, iterations may be necessary to accurately solve the original problem: the optimization can thus be repeated following a standard successive convex optimization approach, where the new trajectory is convexified, until the solution of the optimization and the accurate forward propagation of the maneuvering orbit match to a prescribed accuracy, that is until two consecutive successive iterations yield the same optimization vector. Avoiding successive iterations allows saving computation time, hence an important part of the project was dedicated to the choice of coordinates, which highly impacts the validity of STMs.

<sup>3</sup><https://docs.mosek.com/9.0/toolbox/index.html>

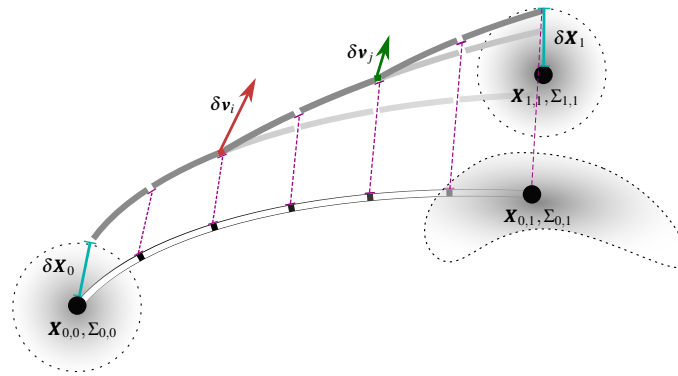


Fig. 5: Initial sampled trajectory (white line with black squares), initial deviation (blue) and mid-course maneuvers (red and green) to match final deviation (blue).

### 3. RESULTS FOR MEV-2

The following analysis was performed on three optical tracks of MEV-2 obtained on 16, 17 and 20 November 2020 by DTA from an observatory located in Auckland. Results for the single track are shown for the first night, while range intersection and maneuver estimation are shown for the window between the 16 and the 20 November 2020.

#### 3.1 Observations regression

Raw optical tracks were firstly interpolated to retrieve their precision. To do so, right ascension and declination were polynomially regressed with respect to time, starting from a linear model, increasing the order until their residuals were randomly scattered. Listings 1 and 2 show respectively the interpolation statistics for right ascension and declination, with a 5<sup>th</sup> order polynomial for right ascension -  $\sigma_\alpha = 2.02$  arcsec -, and a 4<sup>th</sup> order polynomial for declination -  $\sigma_\delta = 1.78$  arcsec. The estimated precision was fundamental to start the ASR and OS algorithms. Figure 6 shows the plot with raw observations and polynomial interpolation.

```

1 Linear regression model:
2   Alpha ~ 1 + Time + Time2 + Time3 + Time4 + Time5
3
4 Estimated Coefficients:
5   Estimate      SE      tStat      pValue
6   -----
7
8 (Intercept)  7.1217  8.7242e-05  81632      0
9 Time         14.913  0.00021667  68830      0
10 Time2       -1.0479  0.00019465  -5383.8     0
11 Time3       0.0059728  0.00027009  22.114     3.3306e-45
12 Time4       0.013973  7.9986e-05  174.69    3.4344e-152
13 Time5       -0.001834  7.6638e-05  -23.931    1.0624e-48
14
15 Number of observations: 132, Error degrees of freedom: 126
16 Root Mean Squared Error: 0.000563
17 R-squared: 1, Adjusted R-Squared: 1
18 F-statistic vs. constant model: 1.91e+10, p-value = 0

```

Listing 1: Polynomial interpolation of right ascension.

```

1 Linear regression model:
2   Delta ~ 1 + Time + Time2 + Time3 + Time4
3
4 Estimated Coefficients:
5   Estimate      SE      tStat      pValue
6   -----
7
8 (Intercept)  7.4454  7.5681e-05  98378      0
9 Time        -0.65933  0.00011096  -5941.9     0
10 Time2       0.028177  0.00015091  186.71     8.0149e-157
11 Time3       0.011698  6.0097e-05  194.66     4.0936e-159
12 Time4       -0.002231  5.4725e-05  -40.772    8.1373e-75
13
14
15 Number of observations: 132, Error degrees of freedom: 127
16 Root Mean Squared Error: 0.000495
17 R-squared: 1, Adjusted R-Squared: 1
18 F-statistic vs. constant model: 5.49e+07, p-value = 0

```

Listing 2: Polynomial interpolation of declination.

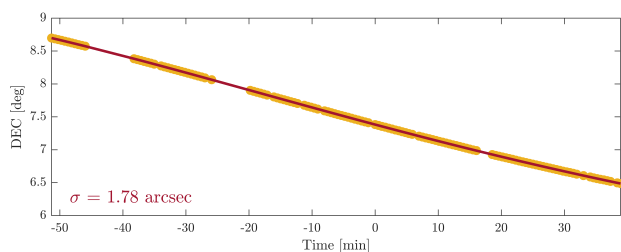
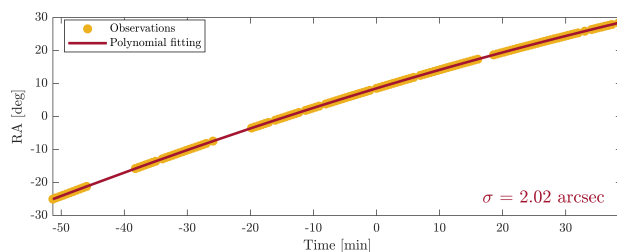


Fig. 6: Polynomial regression of right ascension (left) and declination (right) for the night of the 16 November 2020.

### 3.2 IOD and data association

Once the raw observations and their precision were available, it was possible to build the ASR as described in Section 2.1.1 and the OS as described in Section 2.1.2. Knowing that MEV-2 tracks are much longer than a VSA as seen in Fig. 2, the associated uncertainty is expected to be very small. Fig. 7 summarizes the findings:

- the left plot is the ASR with LS update for the track obtained on 16 November 2020. The initial AR (black lines) was created with  $30000 \text{ km} \leq a \leq 38000 \text{ km}$  and  $e \leq 0.4$ , assuming a certain knowledge on the object. The initial ASR (thick gray lines) was further split when all observations in the track were used to carry out the LS procedure (thin gray lines). It is to be noted that the ASR is shown projected on the 2D AR, however, splits could also be performed in the remaining 4D, which contain the attributable and its confidence interval built on the precision estimated at the previous step. As can be seen, the LS approach pinpoints the solution to a single sub-domain (thick dark gray line). The size of the sub-domain depends on the depth of split and/or accuracy required on the solution. The choice falls on the trade-off between sub-domain size and computing time. Since the final domain is needed to start the association routines, a fast computation of a small initial uncertainty is wished for. For this plot, a maximum depth of split of 8+4 (referring to the initial creation of the ASR and the update with LS) was used, with a wished accuracy of meter level for semimajor axis,  $10^{-4}$  for eccentricity and  $10^{-4}$  rad for all other elements.
- the middle plot shows the OS associated to the same track, with the same accuracy and depth of split as for the ASR. The plot axes are shown in the left plot as well, showing that they fall in the sub-domain identified by the ASR+LS routine. As anticipated in Section 2.1, we expected the two methods to pinpoint the same uncertainty area. The observation domain  $[(\alpha, \delta) \pm 3\sigma] \in \mathbb{R}^6$  could be fully mapped in the state space with a single polynomial, keeping the representation way below the threshold, where  $\sigma$  is the precision estimated through regression in the previous step. The OS was calculated for all three optical tracks. The uncertainty bounds of the resulting OSs in Keplerian elements were then used to look for association.
- the right plot shows the range intersection on the five slowly varying orbital elements for tracks obtained on the 16 (green), 17 (red) and 20 (black) November 2020. Despite a 3D intersection for the OSs obtained on consecutive days, the lack of a 5D intersection means there cannot be a ballistic path connecting the three tracks.

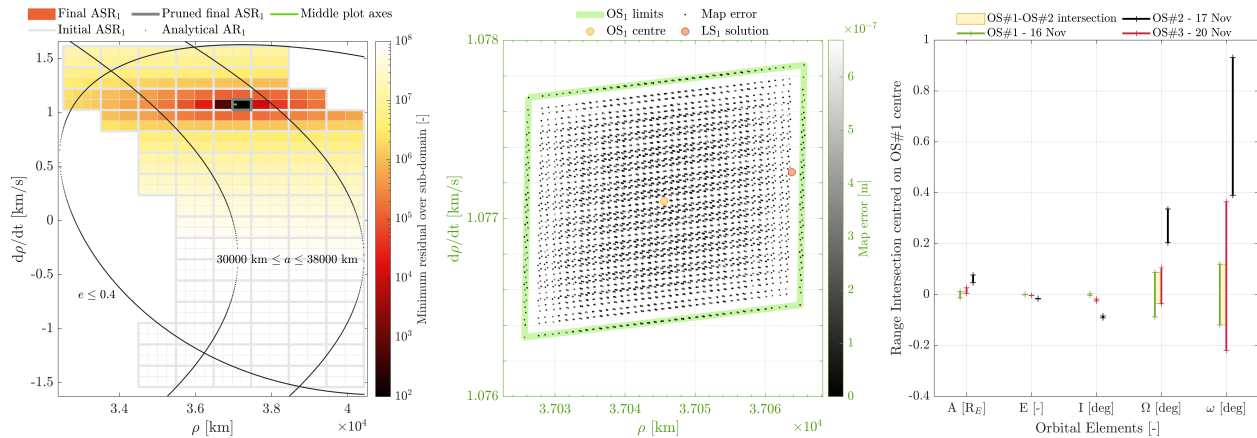


Fig. 7: Results for MEV-2 observations in terms of (a) ASR with LS update, (b) OS and (c) range intersection for observations taken on the three nights.

Each OS with corresponding range intersection took 0.287 s to compute, while the initial ASR took 0.495 s, the update needed 8.480 s and the search for the minima on each subdomain 0.315 s. Unsurprisingly, it is much faster to obtain an OS given the smaller uncertainty region to start with, while the pruning process takes longer. Given the non-correlation result obtained with range intersection, the OSs are independently processed to obtain separate ODs, starting from the OSs centers (the yellow dot in Fig. 7(b)) as initial guess. The solution of the DALs is also plotted on Fig. 7(b) for reference.

### 3.3 OD

To refine the OS solution, the numerical feature of the DALIS using optical observations was used. Figure 8 shows the OD residuals superimposed on the observations precision estimated in Section 3.1, showing agreement on the uncertainty and a scattered cloud of residuals, meaning that the dynamical model captures the observations behavior and does not introduce additional uncertainty.

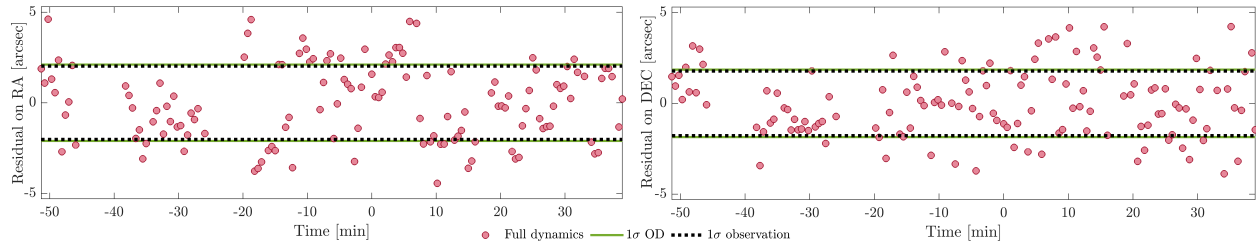


Fig. 8: OD residuals. The uncertainty resulting from the OD and the precision of the observations show good agreement.

The dynamical model used included: Earth’s gravity potential up to order 15, drag with NRLMSISE-00 atmospheric density model, third-body perturbing accelerations - Sun and Moon - with NASA’s SPICE<sup>4</sup> toolkit [1], and SRP with dual-cone shadow model. The numerical propagator Accurate Integrator for Debris Analysis (AIDA) [7], which implements this model, is included in the DALIS and was also used to compute the reference ballistic trajectory for the maneuver estimation. All three tracks from MEV-2 were processed independently with the DALIS. The estimated orbital elements in terms of semimajor axis, eccentricity and inclination are shown in Fig. 9. Here, the OD solution is shown on top of the available Two-Line Elements (TLEs). Furthermore the Simplified General Perturbations 4 (SGP-4) propagator was used to forward propagate each TLE, showing unmodeled “jumps” (dash line). The SPICE TLEs interpolator was also used, and fitting problems are clear (solid line). The fast varying behavior of the elements and difficulty of typical methods to explain it hint at the presence of unmodeled dynamics, i.e. maneuvers.

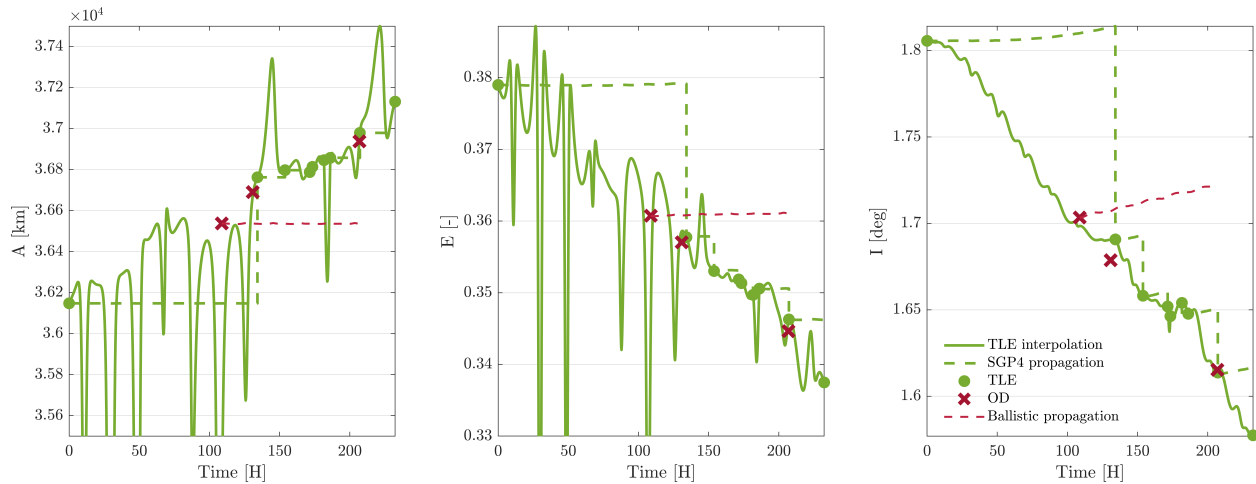


Fig. 9: OD and TLEs show a fast-varying trend in typically slow-varying elements. SGP-4 and SPICE interpolator cannot explain the trend, having jumps and interpolation issues.

<sup>4</sup><https://naif.jpl.nasa.gov/naif/toolkit.html>

### 3.4 Maneuver Estimation

Given the three ODs just obtained, the convex optimization-based maneuver estimator described in Section 2.4 was run to obtain the time-varying orbital elements profile within the observations window, assuming  $a = 2.2 \cdot 10^{-4} \text{ m/s}^2$ . Figure 10 and Fig. 11 show the complete reconstruction for the OD#1-OD#3 window with maneuver profile and statistical analysis, elements evolution, and orbital positioning of the maneuver.

Figure 10 shows the time-profile of the maneuver in RTN components (left), magnitude (top-right) and a-posteriori PDF reconstruction (bottom-right). The bang-bang structure is easy to notice, with the pattern repeating at each period. The  $3\sigma$  uncertainty is noticeable at the verges of the bangs: indeed the state uncertainty influences the start and end times of the maneuvers. The optimal maneuver was obtained with different coordinate systems (cartesian coordinates (CC), COE and modified equinoctial elements (MEE)) all converging to this pattern, however with CC needing successive convexification. The bottom right plot shows the estimated probability density function, boxplot and violin plot of the maneuver magnitude. This was performed by fitting a Pearson distribution in the four momenta - mean  $\mu$ , standard deviation  $\sigma$ , skewness  $s$  and kurtosis  $k$  - exactly reconstructed through the CUT-4. In this case, the statistical analysis informs us that the magnitude of the maneuver is slightly right-tailed, with respect to a typical Gaussian function ( $s = 0$  and  $k = 3$ ). We can then conclude that the use of the CUT-4 algorithm allows for PDF reconstruction without gaussianity assumptions.

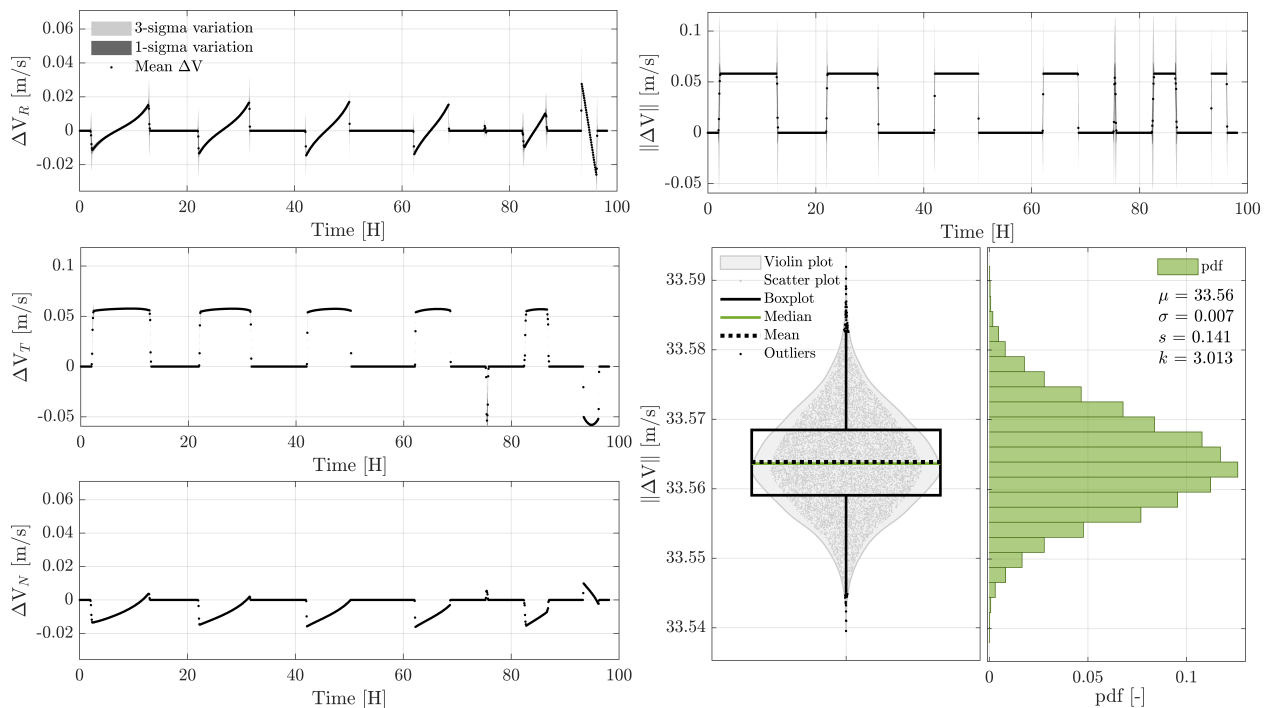


Fig. 10: Time profile of LT orbit raise maneuver by MEV-2 in RTN components (left), time profile of maneuver magnitude (top-right) and a-posteriori PDF reconstruction of total maneuver.

Figure 11 shows the orbital elements evolution superimposed on Fig. 9 on the left, and the orbital positioning of the maneuver in perifocal reference frame on the right. The time-profile of the orbital elements does overlap with OD#2 which was not used to estimate the maneuver but is included to check the accuracy of the profile. It is possible that the satellite was indeed maneuvering while the second track was being acquired, explaining why the profile is not exactly superimposed on the OD. This is the convex solution obtained starting from the accurate ballistic trajectory shown with the red dash. The algorithm convergence is checked with the forward propagation of the estimated maneuver pattern (white dots), which matches with the solution of the convexified problem. Given that a change in the orbit

shape and inclination happened, maneuvers were expected to happen around the line of apsides and the line of nodes respectively, and this is confirmed in the right plot, which shows the evolving orbit.

The STM creation took 9.1 s for 300 nodes, and was used for all 4121 optimizations. Each optimization took on average 0.33 s and was parallelized in MATLAB. The total time necessary to accurately estimate the maneuver and its statistical properties was 5.8 min.

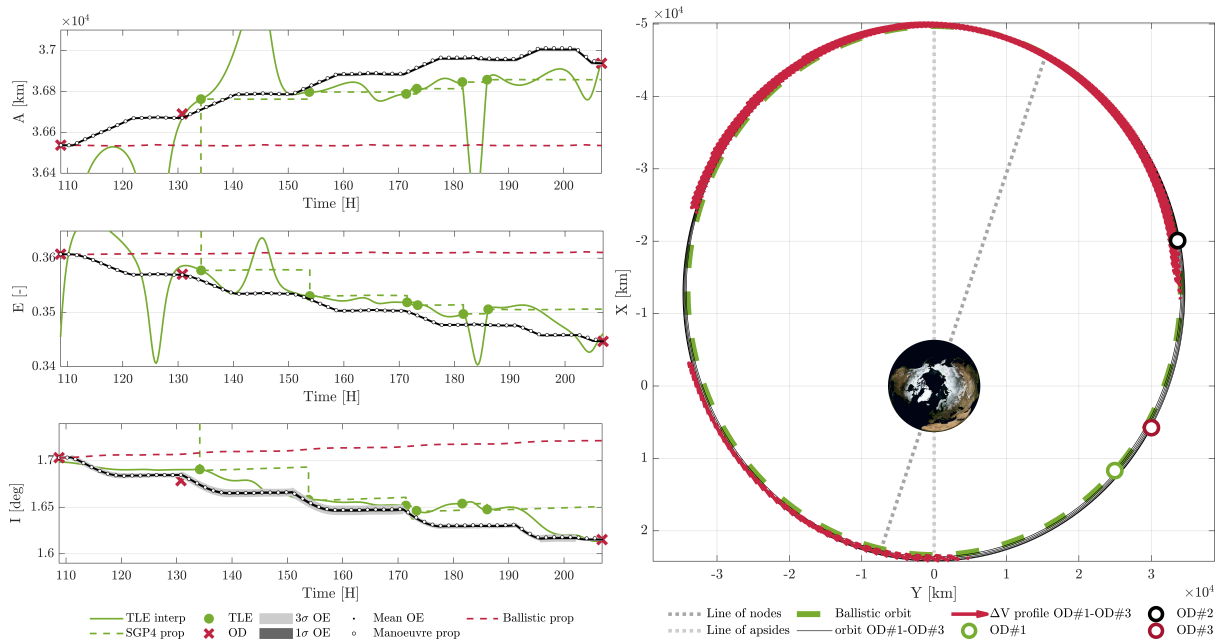


Fig. 11: Time profile of orbital elements variation (left), and maneuvers location along the orbit (right) for LT orbit raise by MEV-2.

#### 4. CONCLUSION

This paper shows the end-to-end capability of the TPA-SI astrodynamics group to take raw optical tracks, perform IOD, data association, OD and maneuver estimation, analyzing some optical tracks of MEV-2 during its LT orbit raise from GTO to GEO. Each tool output served as input to the next task:

- the raw observations were polinomially regressed to obtain the tracks' precision;
- IOD was performed using the observations and their precision in two different ways, leading to the same uncertainty area:
  - An attributable was obtained to generate the ASR, which was then updated with all observations in the track to prune the initial, very large, uncertainty;
  - the list of all orbits fitting in the first, middle and last observations of the track within the precision tolerance was obtained in the form of the OS;
- ASR and OS, being analytical maps, had their uncertainty ranges readily available. They were used to look for a 5D intersection in the slowly varying orbital elements. As expected, the result was the empty set, hence non-correlation, knowing that a LT orbit raise was happening;
- the separate OSs were then fed to the DALs to obtain a refined state and covariance estimate for each track;

- an OCP with uncertain boundary constraints was defined to look for the optimal maneuver profile to connect two ODs. The problem was firstly transformed from a NLP to a SOCP problem to exploit the ensured global convergence and polynomial run time of convex optimization. The CUT-4 algorithm was used to exactly reconstruct four momenta a-posteriori and conclude that gaussianity was not preserved.

Future work will involve automatizing the processes between the algorithms, including parallelization to speed up computation. Regarding the maneuver estimation, future tests will steer towards the usability of the tool for maneuver actuation testing to learn whether a planned maneuver went as expected, or any deviations from the scheduled profile in fact happened. It is indeed possible to have an initial  $\Delta V$  profile in the generating trajectory and estimate any deviations once the maneuver is performed.

## ACKNOWLEDGMENTS

The work presented is supported by AOARD under Grant FA2386-21-1-4115. The authors are grateful to Dr Jovan Skuljan of Defence Technology Agency (DTA) for the provision of data and constructive discussions.

## REFERENCES

- [1] Charles H. Acton. Ancillary data services of nasa's navigation and ancillary information facility. *Planetary and Space Science*, 44(1):65 – 70, 1996.
- [2] Nagavenkat Adurthi, Puneet Singla, and Tarunraj Singh. Conjugate Unscented Transformation: Applications to Estimation and Control. *Journal of Dynamic Systems, Measurement and Control, Transactions of the ASME*, 140(3):1–22, 2018.
- [3] Xinfu Liu, Ping Lu, and Binfeng Pan. Survey of convex optimization for aerospace applications. *Astrodynamics*, 1(1):23–40, 2017.
- [4] Matteo Losacco, Gennaro Principe, Roberto Armellin, Laura Pirovano, David Gondelach, Juan Felix San Juan, Martin Lara, Raul Dominguez Gonzalez, Fernando Pina Caballero, and Igone Urdampilleta. Differential Algebra-based Orbit Determination with the Semi-analytical Propagator SADA. *8th European Conference on Space Debris*, april 2021.
- [5] Danylo Maluyuta, Taylor P Reynolds, Michael Szmuk, Thomas Lew, Riccardo Bonalli, Marco Pavone, and Behçet Açı kmeşe. Convex optimization for trajectory generation. *arXiv preprint arXiv:2106.09125*, 2021.
- [6] Andrea Milani, Giovanni Gronchi, Mattia de' Michieli Vitturi, and Zoran Knezevic. Orbit determination with very short arcs. I admissible regions. *Celestial Mechanics and Dynamical Astronomy*, 90(1-2):59–87, 2004.
- [7] Alessandro Morselli, Roberto Armellin, Pierluigi Di Lizia, Franco Bernelli-Zazzera, P. Di Lizia, and Franco Bernelli-Zazzera. Collision avoidance maneuver design based on multi-objective optimization. In *24th AAS/AIAA Space Flight Mechanics Meeting*, volume 152, 2014.
- [8] Laura Pirovano, Roberto Armellin, Jan Siminski, and Tim Flohrer. Differential algebra enabled multi-target tracking for too-short arcs. *Acta Astronautica*, 182:310–324, 2021.
- [9] Laura Pirovano, Daniele A. Santeramo, Roberto Armellin, Pierluigi Di Lizia, and Alex Wittig. Probabilistic data association: the orbit set. *Celestial Mechanics and Dynamical Astronomy*, 132(2):15, 2020.
- [10] Laura Pirovano, Daniele A. Santeramo, Roberto Armellin, Pierluigi Di Lizia, and Alexander Wittig. Probabilistic data association based on intersection of orbit sets. In *19th AMOS Conference, September 11-14, 2018, Maui, USA*. Maui Economic Development Board, Inc., September 2018.
- [11] Alexander Wittig, Pierluigi Di Lizia, Roberto Armellin, Franco Bernelli Zazzera, Kyoko Makino, and Martin Berz. An automatic domain splitting technique to propagate uncertainties in highly nonlinear orbital dynamics. *Advances in the Astronautical Sciences*, 152:1923–1941, January 2014.